Oxidation of tungsten at room temperature irradiated by oxygen plasma

Meral Sharkass[1], Swarit Dwivedi[2], Yun Kyung Shin[2], Martin Nieto-Perez[1], Adri van Duin[2] and Predrag S. Krstic[3,4,]*

[1]Ken and Mary Alice Lindquist Department of Nuclear Engineering, The Pennsylvania State University, University Park, Pennsylvania 16801, United States.

[2]Department of Mechanical Engineering, The Pennsylvania State University, University Park, Pennsylvania 16802, United States

[3]TheoretiK, Port Jefferson Station, NY 11776, USA

[4]Department of Material Science and Chemical Engineering, Stony Brook University, Stony Brook, NY 11794, USA

ABSTRACT

The performance of tungsten as a fusion material depends on its surface properties, which are strongly affected by the interaction with impurities, either already contained in the bulk or coming from the plasma. Plasma-facing components, such as the divertor and the first wall of the current fusion reactors, as well as many of the laboratory experiments, are operating at or are cooled down

*Corresponding author: krsticps@gmail.com

to room temperatures. We performed a detailed molecular dynamics study of the processes of oxidation of a tungsten surface at 300 K when it was cumulatively irradiated by a low-energy oxygen plasma. We developed and used a ReaxFF W-O-H classical potential, capable of treating reactive interactions of all atoms in the system, including polar interactions present when O interacts with tungsten. We also studied the properties of the oxidized layers and their response in the form of reflection, retention, and chemical sputtering to the impact of oxygen.

Keywords: Molecular dynamics, ReaxFF, oxygen plasma, tungsten oxidation, reflection, retention, sputtering.

1. INTRODUCTION

Tungsten is a prime candidate for plasma-facing components (PFCs) in fusion reactors. Being a refractory metal, W exhibits exceptional high-temperature properties, making it an attractive material for components exposed to the extreme conditions of fusion plasma [1-3]. Of all metallic elements, W has the highest melting point (3422 ℃), and at elevated temperatures, it exhibits the highest tensile strength among metals [4-5]. Additionally, W shows exceptional corrosion resistance and is highly resistant to attacks by mineral acids. An important advantage of W is its high threshold energy of sputtering, around 150-200 eV for Deuterium (D) [6-7], which helps minimize wall erosion. However, erosion could also occur due to unavoidable impurities, which reduce the threshold value of the D sputtering energy [8]. For example, the threshold energy for the sputtering of W-oxide by D is as low as 65 eV [9] due to the low binding energy of the W-O molecules. Tungsten erosion poses a significant challenge for fusion reactors, as it can impact the lifespan of plasma-facing materials and the overall performance of the reactor. Additionally, the

plasma impurities resulting from the erosion of plasma-facing materials (PFM) lead to a decrease in plasma temperature and power losses and ultimately to plasma turn off. A very small percentage of 0.052% tungsten in the core of the D-T fusion plasma would completely disrupt the fusion process [10].

Oxygen is an ubiquitous impurity in fusion plasma, as demonstrated by ultraviolet spectroscopy measurements conducted in the WEST tokamak [11-12]. Because it is impossible to eliminate O impurities from a large vacuum vessel, plasma-facing components will unavoidably suffer from enhanced erosion. Since W has a high affinity for O, O-containing impurities play a role in tungsten erosion and contribute to an increase in its sputtering yield [13]. Furthermore, when addressing the presence of O, chemical sputtering of W becomes a significant concern [14]. This process occurs when surface atoms react with impacting ions or atoms, creating molecules weakly bound to the surface that are easily released into the gas phase. The introduction of low-energy O atoms to the surface of W will lead to the formation of tungsten oxides (WO_x). A complete description of the interaction between W and O is crucial, given the significant electronegativity difference between the two elements (2.36 for W and 3.44 for O), resulting in the formation of WO_x. This interaction profoundly influences the performance and reliability of tungsten PFC's. Consequently, reactor designers must account for the presence of plasma impurities, particularly oxygen, and their effects on tungsten.

Previous publications focused on the study of W oxidation from the perspective of accidents such as cooling loss (LOCA) and vacuum loss (LOVA) [15-16] or from W oxidation at high temperatures. In such accidents, the temperature of W can increase to 1500 K [17] in addition to the air ingress into the vacuum vessel, resulting in severe oxidation of W due to the high metal temperature and the presence of O. Previous research work studied experimentally and

theoretically the effect of chemical sputtering of O on W erosion at temperatures of 1500-2000 K at different O pressures [7, 12, 18, 19]. The introduction of an adequate amount of O to the tungsten surfaces results in the chemical sputtering of WO_x molecules, thereby reducing the threshold energy for sputtering with D. W sputtering by D was observed in the presence of 10^{-2} Pa of O_2 gas at energies below the D-W sputtering threshold [20].

W oxidation has been observed at temperatures below 1500 K, even at room temperature [5, 21]. W-based PFCs in ITER and other fusion reactors are actively cooled to room temperature, motivating lab-based experiments performed at ambient temperatures. Because existing studies, to the best of our knowledge, have primarily concentrated on W oxidation at high temperatures, the understanding of the oxidation of tungsten at room temperatures, especially when impinged by nonthermal oxygen atoms, is limited. In this work, we study the creation of surface W oxides at room temperature when irradiated by energetic O atoms (1-30 eV), as well as their properties including the effects on chemical sputtering of W.

In Section 2, we report on the development and properties of a new Reactive Force Field (ReaxFF) parameter [22-25]. It should be noted that prior to our study, a classical W-H-O interaction potential, which would utilize their mutual polarization features, had not been generated. Our work introduces a novel ReaxFF parameters to address this gap in the literature. Our classical molecular dynamics (CMD) methodology, including preparation of the tungsten surface target, is described in Section 3. In Section 4, we present and analyze the CMD results of the surface evolution of W-O due to cumulative O impacts at various energies. The conclusions of our study are given in Section 5.

2. DEVELOPMENT OF REAXFF FORCE FIELD PARAMETERS

The Reax Force Field, ReaxFF, is a bond order-based computational approach used in molecular dynamics simulations to model the potential energy space of atomic models. In general, standard molecular mechanics force fields are insufficient to describe chemical reactions, because of their inability to simulate bond formation and breaking. However, in ReaxFF, the energy contributions from bonded interactions, such as bonds, angles, torsions, etc., are calculated as functions of the bond order, which is dynamically calculated based on the interatomic distance. ReaxFF parameters also include non-bonded interactions, such as van der Waals forces and Coulombic (electrostatic) interactions. A detailed discussion on the transferability and training of ReaxFF parameters can be found elsewhere [22, 24]. As is the case with empirical force fields, ReaxFF is trained to reproduce physical and chemical space as either observed in experiments or calculated by reliable quantum mechanics (QM) -based methods. The force field training objective is to minimize the error function defined in Eq. 1,

$$\boldsymbol{Error} = \sum_{\boldsymbol{i=1}}^{\boldsymbol{n}} \left(\frac{\boldsymbol{X_{i,QM} - X_{i,ReaxFF}}}{\boldsymbol{\sigma}} \right)^{\boldsymbol{2}} \quad (1)$$

Here $X_{i,QM}$ is the reference data (experiment or QM) and $X_{i,ReaxFF}$ is the corresponding value of ReaxFF and σ is the accuracy parameter (inverse of training weight) for the i-th data. In the single-parameter search optimization scheme, one force field parameter at a time is varied by a small amount to minimize the overall error (Eq. 1) in the training data. This method is further described by van Duin et al.. [26], and is implemented in the standalone ReaxFF code, which can be made available on request [27].

The reference data for force field training ($X_{i,QM}$) are collected from the following three sources, a) previously published QM results [28-31], b) experimental data [32], and c) Density Functional Theory (DFT) simulations performed in this work. We performed periodic and molecular DFT

simulations to calculate energies, atomic charges, and geometric parameters, including Equation of States (EOS), Heats of Formation (ΔH_f), and pair potentials. Molecular DFT (pair potentials, bond scans, and angle scans) simulations were performed using the Amsterdam Density Function (ADF) code [33] within the Amsterdam Modelling Suite (AMS) [34]. We performed spin-polarized calculations with generalized gradient approximation (GGA) based Perdew-Burke-Ernzerhof (PBE) exchange correlation functionals in combination with the TZP base set (triple Z with 2 polarization function) [35, 36].

To simulate periodic structures, we performed DFT simulations using the Vienna ab initio software package (VASP) [37, 38]. We used spin-polarized calculations with the generalized gradient approach based on the Perdew-Burke-Ernzerhof (PBE) exchange-correlation pseudopotential [35] with a plane wave cutoff of 520 eV. Grimme's DFT-D3 method [39] with a zero-damping function was used to add a correction term for the dispersion energy. Partial occupancies for each orbital were set using the tetrahedron method with Blöchl corrections of smearing width 0.05 eV. A Gamma-centered 10×10×1 K-point mesh was used for all simulations. We ensured a vacuum of 20 for the slab-based structures to avoid interaction with periodic images. We use the conjugate gradient algorithm to minimize the overall energy with a maximum error of 5×10^{-4} eV.

Table 1 presents a comparison of ReaxFF calculations for tungsten BCC lattice and W-dimer against experiments, first-principles calculations, and two of the widely used bond order-based potentials in the field of fusion materials (Li et al. [40] and Juslin et al.. [41] The valence force field parameters for tungsten (W-W-W) were trained. We followed the training methodology presented by Shin et al. [42] to obtain a good agreement between ReaxFF and DFT [43, 44] for the strain - energy relationship (supporting material (SM), Fig. S-1).

Table 1: Comparison of ReaxFF energies relevant for W-atom parameters.

	ReaxFF	Experiments	First-principles	Li et al. [40]	Juslin et al.. [41]
W (BCC)					
E_C	-8.846	-8.9 [48]	-7.4061[40]	-8.906	-8.89
a	0.3172	0.3165 [49]	0.318 [50]	0.3165	0.3165
B	305.21	308-314 [51]	305-320 [50,52]	307	308
C11	502.84	501-521 [51]	522 [52]	515	542
C12	206.42	199-207 [51]	204 [52]	203	191
C44	140.82	151-160 [51]	149 [52]	162	162
E_{vf}	3.97	3.7 ± 0.2 [54]	3.11-3.56 [50, 54]	3.52	1.68
E_{vm}	1.84	1.8±0.11 [54]	1.66-1.78 [50, 54]	1.81	1.77
E_{SIA} *d-100*	8.1		11.49-11.74 [50, 54]	12.01	8.93
E_{SIA} *d-110*	8.2		9.84-10.10 [50, 54]	9.53	8.77
E_{SIA} *d-111*	8.54	9.06 [32]	9.54-9.82 [50, 54]	9.33	9.62
E_{SIA} *(t)*	9.18		11.05-11.99 [50, 54]	10.75	8.6
E_{SIA} *(o)*	9.52		11.68-11.64 [50, 54]	12.05	9.92
W-W Dimer					
E_C	-2.03	-2.5 [53]	-2.05 [40]	-1.44	-2.71
r_0	0.265	0.221 [53]	0.195 [40]	0.239	0.234

E_C = cohesive energy, a = lattice constant (Å), B = bulk modulus (GPa), C_{ij} = stiffness coefficient (GPa), E_{vf} = Vacancy formation energy (eV), E_{vm} = Vacancy migration energy barrier, E_{SIA} = Self-interstitial formation energy (eV), d-ijk = dumbbell along the ijk direction, t = tetrahedral, o = octahedral. r_0 = length of the equilibrium bond in nm. All energies are in eV.

Fig. 1 shows cases of the comparison between ReaxFF and DFT for structures with W and H atoms. Fig. 1a shows the atomic charges calculated by the EEM method [45] in ReaxFF and Mulliken charges as calculated by PBE-DFT in this work for the WH_4 molecule, while Figs. 1b

and 1c present a comparison of the W-H bond scan and the H-W-H valence angle scan for the same molecule.

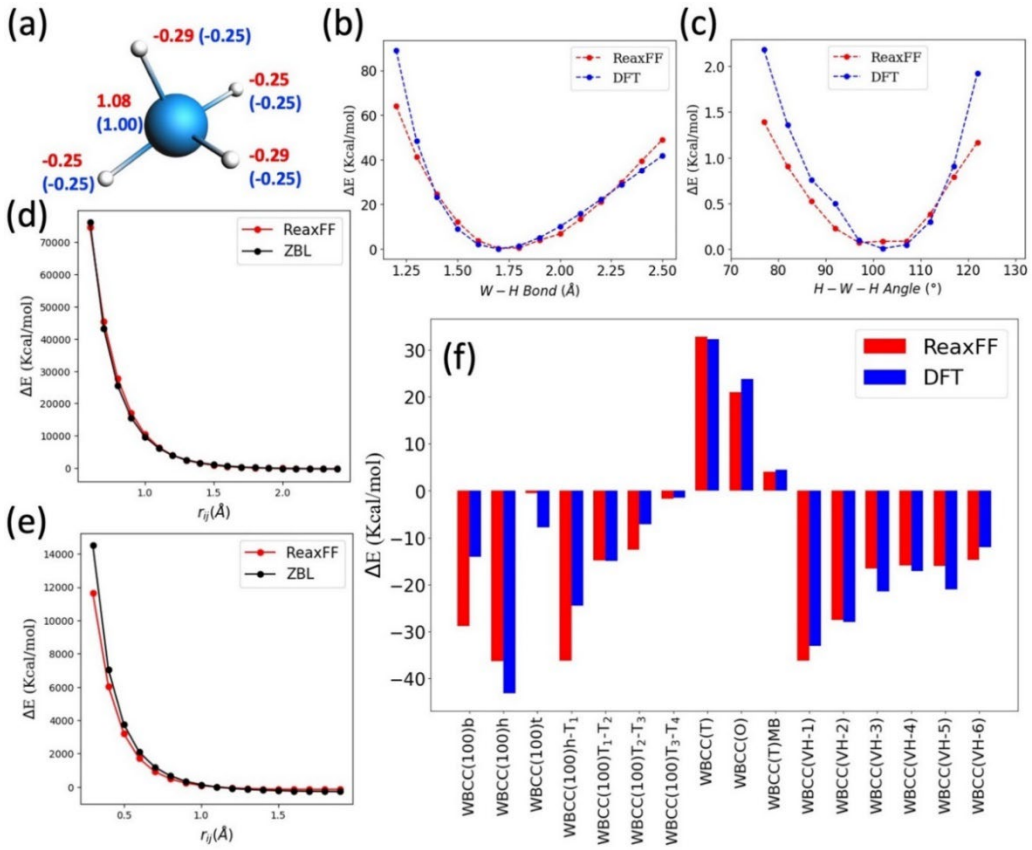

Figure 1: (a) Atomic charges on the WH_4 molecule calculated by ReaxFF (DFT). (b) and (c) show the energy change in varying the length of the W-H bond and H-W-H valence angle in WH_4 molecule. (d) and (e) show the pair potentials between W-W and W-H, respectively. (f) Comparison between ReaxFF and DFT for various binding sites of H in a W-BCC crystal. b=bridge, h=hollow, t=top, T=tetrahedral, and O=octahedral interstitial, Ti=tetrahedral interstitial at i^{th} subsurface, (T)MB = migration barrier between two tetrahedral sites, VH-i = i^{th} H atom near a vacancy.

Close-range interactions are crucial for simulating high-energy impact. However, DFT often yields erroneous results for small distances [46]. Therefore, the close-range encounters for W-W

and W-H atom pairs are trained on the ZBL potential [47], as shown in Fig. 1-d and Fig. 1-e, respectively. Fig. 1-f presents the energetics of H atoms in the body-centered cubic lattice of tungsten.

The trained energies encompass adsorption of H on a BCC (100) W surface (top, bridge, and hollow sites), interstitial H at the tetrahedral and octahedral sites, the energy difference between surface adsorbed H and subsurface H atom at the tetrahedral site, and binding of H to a tungsten vacancy site in the lattice.

Fig. 2 compares the ReaxFF calculations with the reference data for relevant systems containing W and O atoms. Fig. 2-a shows the atomic charges calculated by the EEM method in the ReaxFF and Mulliken charges calculated by PBE-DFT in this work for WH_3 and $WO_2(OH)_2$ molecules, while Fig. 2-b shows the same comparison for the W-O bond scan in the $WO_2(OH)_2$ molecule. Fig. 2-c shows the pair potential for the pair of W - O atom pair; the close-range potential (<0.6 Å) for the reference curve is calculated using the ZBL potential, while PBE-DFT is used for distances > 0.6 Å. The two most stable WO_3 lattices are orthorhombic and tetragonal, and Figs. 2-d and 2-e show their equations of state (energy vs. volume relationship), respectively. The heats of formation (per atom) for the WO_2, WO3 and $W_{18}O_{49}$ lattices are given in Fig. 2-f. Upon irradiation of W with O atoms, the formation of a WO_x surface is likely, and the surface energy of the WO_3 lattice is thus an important chemical space that we cover by training against the surface energies of the WO_3 tetragonal and orthorhombic lattices along with the stable surfaces of W-BCC (Fig. 2-g). In the event of sputtering, stable molecules of WO_x are expected to form, and we train the formation energies of stable oligomers of tungsten oxides with respect to the WO_3 molecule (Fig. 2-h).

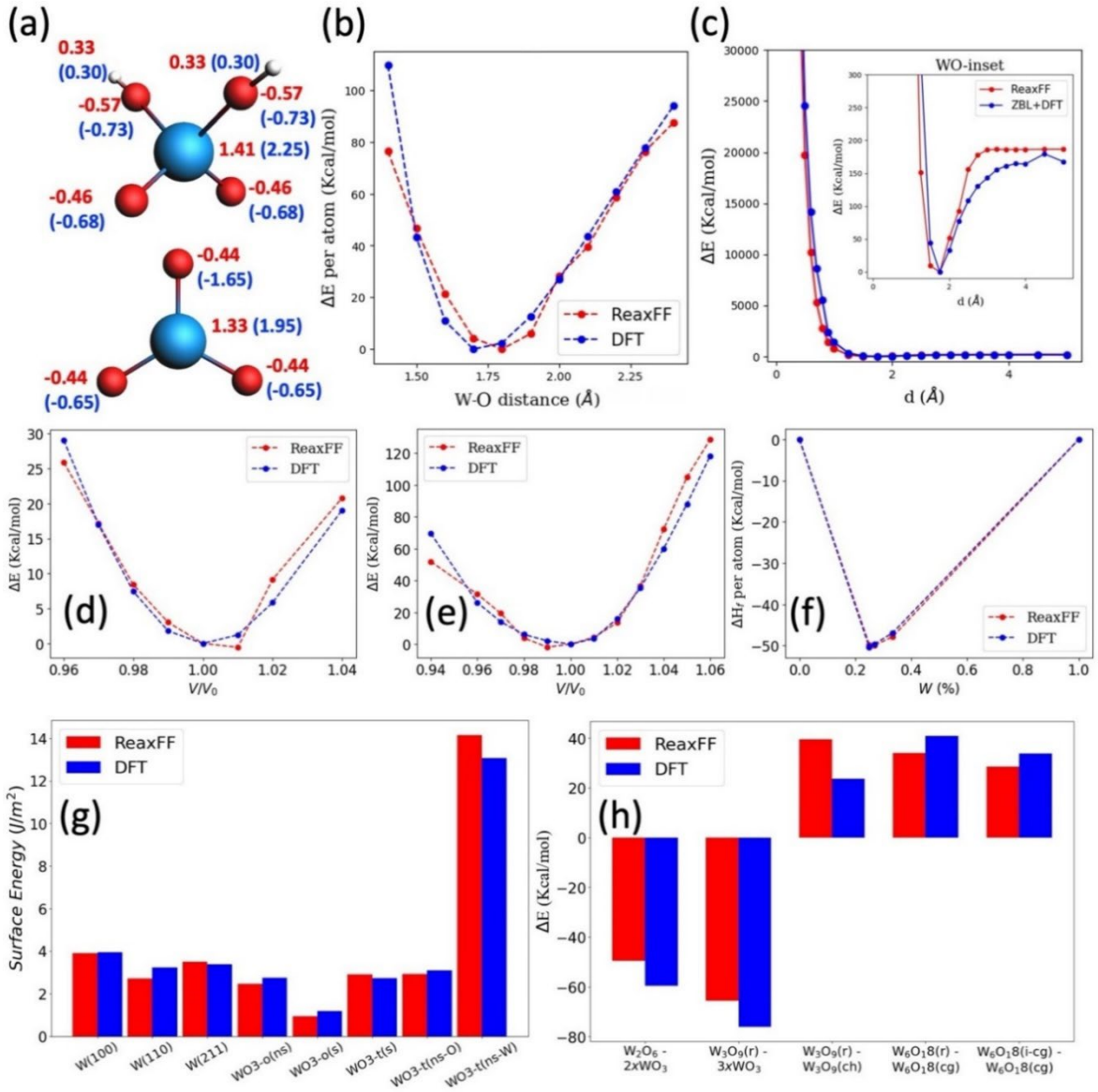

Figure 2: (a) Atomic charges in WO_3 and $WO_2(OH)_2$ molecules calculated by ReaxFF (DFT). (b) Energy changes with the variation of the length of a W-O bond in a $WO_2(OH)_2$ molecule. (c) Pair potential between W-O, and inset shows a near equilibrium region. (d) and (e) Equations of the state of the tetragonal phase WO3 and orthorhombic phase WO3, respectively. (f) Convex hull (ΔH_f per atom) for the stable oxides of tungsten. (g) Surface energies of W and WO_3 orthorhombic surfaces. (h) Energy difference between various stable gas-phase molecules of W and O. r = ring, ch=chain, cg = cage, and i-cg = inverted cage.

3. SURFACE PREPARATION AND MD METHODOLOGY

We conducted classical molecular dynamics simulations using the newly developed ReaxFF potential [22-25], described in Section 2, adapted for a mixture of W-H-O materials. Simulations were implemented using the LAMMPS MD simulator [55] running on high performance computing (HPC) infrastructure at UC San Diego [56] and Pennsylvania State University [57]. We started the modelling by creating a 28×28×84 $Å^3$ mono-crystalline BCC tungsten structure with a lattice constant of 3.1652 Å, containing 4374 atoms. The surface plane of the lattice was [001]. The bulk crystal was energy-minimized and slowly thermalized to 300 K under 3D periodic boundary conditions (PBCs), using a Langevin thermostat. Subsequently, the PBCs were removed from the z-direction to create a 2D periodic slab. The system was rethermalized at 300 K and then equilibrated for 0.5 ps to allow slab relaxation and stabilization. Three identical W slabs were irradiated sequentially and cumulatively by 4500 incident oxygen atoms each, with incident energies 1, 10, or 30 eV, respectively, randomly choosing a point of impact. The impact energies were selected to explore the effects of oxide creation with low- and high-energy oxygen coming from the plasma. The energies of the oxygen atoms were below the physical sputtering threshold of ~ 40 eV for W by O [7, 8]. The O atoms were placed in the negative z direction, perpendicular to the top surface of the W slabs every 4 ps for incident energies of 10 and 30 eV and every 3 ps for 1 eV, as shown in the initial setup of the system, Figs. (3-a) and (3-a'). A buffer zone of 5 Å was maintained in the x and y directions of the top surface to avoid overlap of periodic border interactions, resulting in an active deposition area of 23×23= 529 $Å^2$.

The timestep through all the simulations of the W-O systems was 1 fs. This time step exhibited a good resolution to observe reflection and sputtering incidences for all three O impact energies. The total number of time steps for each O impact was 3000 for 1eV energy and 4000 for 10 and

30 eV impact energies. Each O impact caused a collisional cascade on the picosecond time scale, and the surface processes were allowed to evolve without forced exchange of energy with the environment. After incident O atom thermalization due to the collisional cascade, the entire system underwent a cooling to 300 K by applying the Langevin thermostat for 0.5 ps, which dissipated any excess heat resulting from an impact and emulated the natural or forced cooling process occurring over much longer timescales. The cooling step was imperative due to the disparity in time scales between molecular dynamics simulations (ranging from femtoseconds to nanoseconds) and real experiments, where the irradiation flux is usually many orders of magnitude smaller, allowing cooling to a desired average temperature of the slab. The simulation process produced the oxygen irradiation fluence of 8.5×10^{20} atoms/m^2 after 4500 atom impacts. The deposition flux was 2.83×10^{32} atoms/m^2sec for the 1 eV O impact energy case and 2.1×10^{32} atoms/m^2sec for the 10 and 30 eV incident energy cases.

We conducted an additional series of simulations to explore the instantaneous surface processes while irradiating tungsten oxide with oxygen. The objective was to examine the sputtering of W and O and reflection dynamics upon single O impact on preoxidated W slabs during the irradiation process. To achieve this, we employed two types of slabs derived from previous accumulation simulations: one with 200 O deposits for all incident energies (low oxygen irradiation) and the other with 500, 900, and 1200 O deposits resulting from cumulative O impacts of 1, 10 and 30 eV on W slabs, respectively (high oxygen saturation). We designate the three low oxygen irradiation scenarios as *"A-deps"* and the three high oxygen saturation scenarios as *"B-deps"*. Each slab was then exposed to 1000 non-cumulative O-atom bombardments matching their respective accumulation energy, randomly varying the position of the atom impact. For example, slabs resulting from 1 eV O accumulation were irradiated with individual O atoms at 1 eV, while those

from 10 eV and 30 eV accumulations underwent O impacts at 10 eV and 30 eV, respectively. This systematic approach facilitated a comprehensive exploration of instantaneous O sputtering and reflection dynamics at various levels.

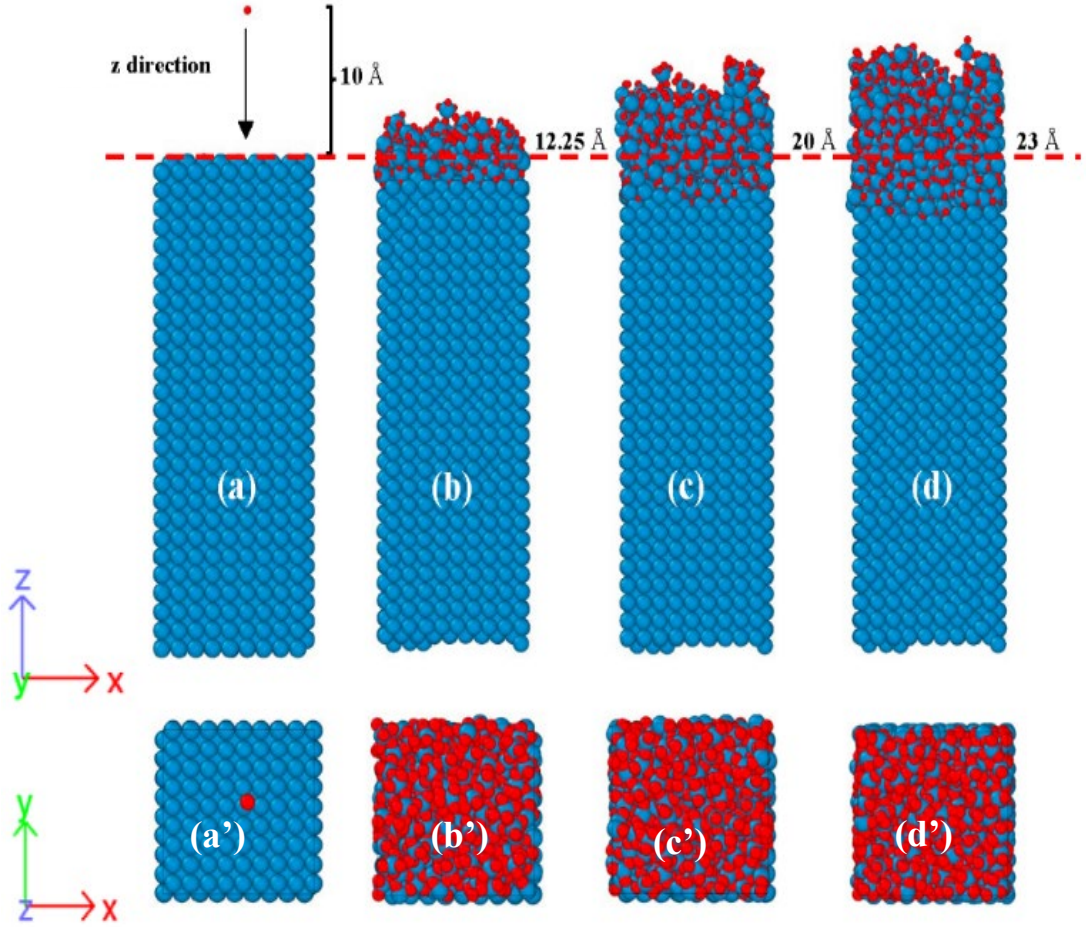

Figure 3: W substrates at the beginning and end of the O accumulation process. **Blue:** W, **Red:** O. **Red line:** Original tungsten surface before accumulation of O. (a) Initial W substrate, (a') planar view for the initial W sample, (b) 500 O deposits with initial energy of 1eV, (b') Planar view of the W slab after accumulation of 500 O deposits, (c) 900 O deposits with an initial energy of 10eV. (c') Planar view of W slab after accumulation of 900 O deposits, (d) 1200 O deposits with initial energy of 30 eV, (d') planar view of W slab after accumulation of 1200 O deposits.

4. RESULTS

4.1 *Creation and properties of tungsten oxide layers*

The impact of O at various energies (1, 10, and 30 eV) on the surface of the monocrystal W resulted in the formation of ad atom layers composed of O and W due to the low solubility of O in W and the small value of the O diffusion coefficient [21]. Although O atoms penetrated W for all three energies, the majority contributed to the formation of an ad layer on the top of the W surface. Moreover, the created O ad-atom layers are mixed with W atoms, which diffuse from the W surface, creating mixed layers of WO_x. The formation of O ad layers on a surface of W, containing mixed O and W, is consistent with previous experimental studies [58, 59].

The irradiation of W surfaces was performed by 4500 O atom impacts with energies 1, 10 and 30 eV. These resulted in ad layers of O-W of 12.25, 20, and 23 Å thicknesses, respectively. The saturated layers are shown in Figs. (3-b,b'), (3-c,c') and (3-d,d'). The W slab irradiated by 4500 O atoms of 1 eV absorbed approximately 570 O deposits before saturation; any additional influx of O atoms resulted in significant sputtering and reflection of oxygen. In other words, the formed ad layer reached saturation of O and most of the subsequent O impacts were either reflected in the vacuum or caused sputtering of ad layer atoms or chemical sputtering of molecules, as will be shown later.

For exposures to incident O atoms with energies of 10 and 30 eV, approximately 900 and 1200 O atoms were deposited, respectively, before reaching saturation of the ad layer. Fig. 4-a shows the relation between irradiation and deposited fluence. Therefore, a W slab bombarded with 1 eV approached saturation at irradiation fluence of 2.25×10^{20} O atoms/m^2 equivalent to approximately 1500 O impacts, while slabs bombarded with 10 and 30 eV reached saturation at irradiation fluences of 6.0×10^{20} (3,300 impacts) and 2.8×10^{20} O atoms/m^2 (1800 atoms), respectively. The

saturation corresponded to deposits of 900 and 1200 O for 10 and 30 eV, respectively. This can be observed at Fig. 4-b, where the number of ejected O atoms (reflected +sputtered) for each 100 impacts stays on average close to 100 after reaching saturation.

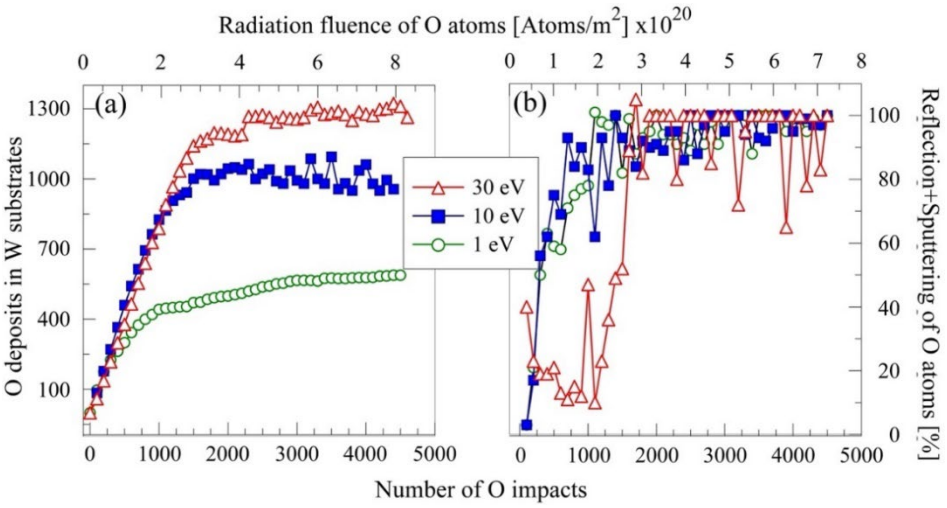

Figure 4: (a) Number of O deposits versus O irradiation fluence (number of impacts) on the W surface (b) Reflection + sputtering of O atoms versus O radiation fluence.

As expected, O atoms with impact energies of 10 and 30 eV exhibited greater penetration through the ad layer into the W surface compared to the 1 eV O atoms, as shown in Fig. 5. As a result, W slabs irradiated by 10 and 30 eV O atoms could accommodate more O atoms deeper into the W surface before reaching O saturation, unlike the impacts by 1 eV O atoms, which had difficulty penetrating the oxide ad layer to reach the W surface. This observation highlights the difference in O saturation points between 1 eV and the higher-energy O atoms under study but also indicates that the growth of the oxide ad-layer evolves outwards from the W surface.

Fig. 5 illustrates three distinct regions of the W oxide. The "*ad-layer*" region (shown in red in the figures) represents the layer above the original W surface, comprising both W and a relatively high concentration of O. The second region corresponds to the W "*bulk*" (shown in black), which consists solely of W. The third region, defined as the "*Boundary between Ad-layer and Bulk (B-A-*

B)" region (depicted in green), was located below the original W top surface, containing a mixture of W and O.

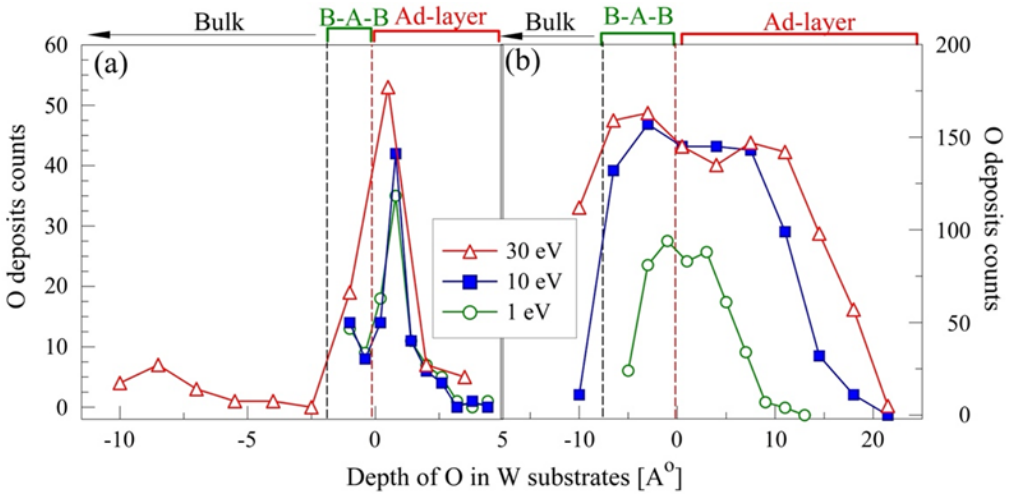

Figure 5: Histograms of the O profile on the W slab along the z-axis for impact energies of 1, 10 and 30 eV: (a) A-deps slab and (b) B-deps slab. The red dashed lines indicate the boundary between the ad layer and B-A-B regions, while the black dashed lines indicate the boundary between the B-A-B and bulk regions.

The comparisons of the onset and the final O depth profiles for the three energies studied in Fig. 5, show histograms of the counts of O atoms in the z-direction of the three O impact energies, for

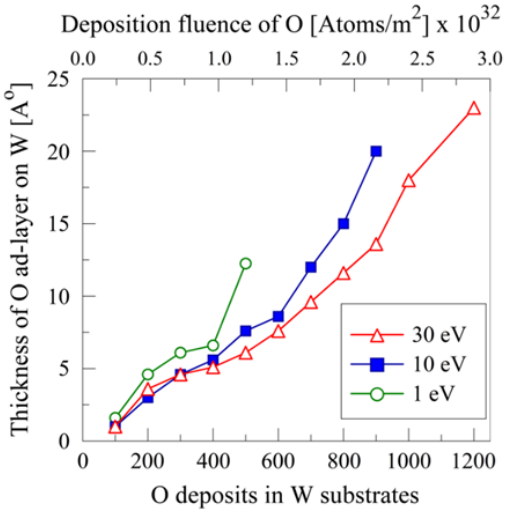

Figure 6 Increase in the thickness of the additional layer with the number of O deposited.

The A-deps (Fig. 5a) and B-deps (Fig. 5b) slabs. For the A-deps slabs, it is evident that most of the impacting O atoms form an ad layer over the W surface, penetrating less than 2 below the surface. However, at the end of the accumulation (Fig. 5b), the penetrated O atoms are distributed up to 5, 10, and 13 Å the W for impact energies 1,10 and 30 eV, respectively. Fig. 6 shows the increase in the thickness of the ad layer during irradiation by O, with increasing the number of deposited O atoms.

For a more comprehensive analysis, we divided the W slab into bins in the negative z direction, each containing roughly 200 oxygen deposits (equivalent to approximately 3 to 3.5 bin thickness). Fig. S-2 in the supporting material shows a visualization of the bins.

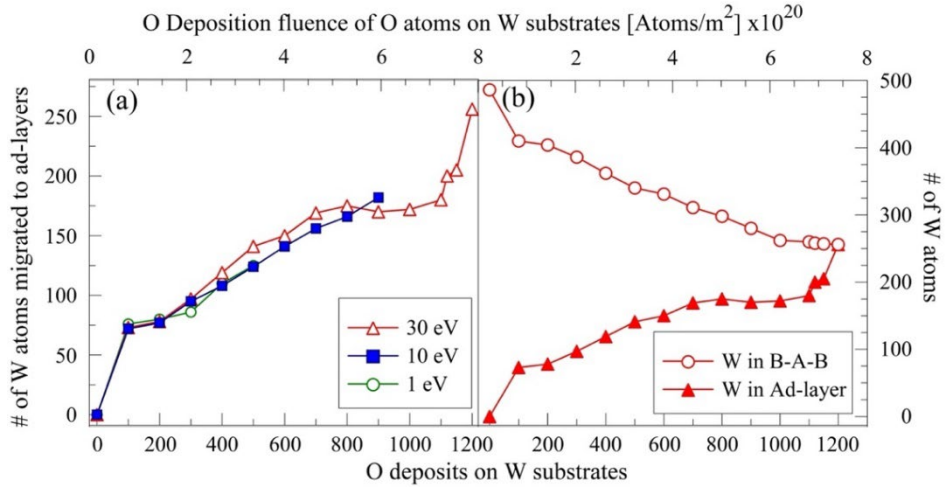

Figure 7 W atom migration from the bulk to the add-on layers. (a) W atoms in the ad layers of impact energies of 1, 10 and 30 eV. (b) Decrease of W atoms 9Å below the ad layer (B-A-B region) and simultaneous increase of W atoms in the ad layer.

configurations resulting from the three O impact energies. Before the accumulation process, there were no ad layers and no W atoms above the original top W surface. As a result of the oxygen

accumulation processes, the presence of W atoms above the original W surface is visualized in Fig. 7. Fig. 7-a shows the number of W atoms migrated from the bulk to the ad layers for 1, 10 and 30 eV impact energies. A detailed analysis of W counts per bin in the ad layer and B-A-B regions is shown in Fig. 7-b for 30 eV impact energy as an example. The number of tungsten atoms near the top W surface (in the B-A-B region) decreased, and a consecutive increase in W counts occurred in the bins of the ad layers.

To understand the dynamics of O accumulation, we studied the n_O/n_W ratio along the thickness of the slab + ad layer, shown in Figure 8. Bins of 200 atoms, as previously illustrated in Figure S-2, were utilized. We found that the n_O/n_W ratios for the 1, 10 and 30 eV cases were larger than 3 in the higher top of the ad layers, indicating a high buildup of O on the surface of W at the beginning of the accumulation process. However, in the B-A-B region, the ratio was 1.7:1. We also observed an increase in the n_O/n_W ratio throughout the W and ad-layers as a function of the z coordinate. This ratio reaches 3 at the upper part of the ad layers, typical for WO_3. The B-A-B regions exhibit lower n_O/n_W ratios. The higher bins (Bin 5 for 30eV, Bin 4 for 10eV, and Bin 3 for 1eV in Fig. S-2) exhibit the highest n_O/n_W ratios compared to the lower bins. Within the ad layer, as we get closer to the original surface, this ratio decreases, but for all ad layer bins, the ratio is always $\geq$ 3:1. Detailed results are illustrated in Table S-1 of SM and Fig. 8. Additionally, the n_O/n_W ratio on the B-A-B layer decreases to 2:1 in the bins close to the original top surface of W and decreases further as we go deeper into the bulk of W. Obtaining n_O/n_W ratios of ~2 near the bulk W and ~3 in the ad layers aligns well with the existing literature [5, 60, 61]. Oxygen atoms move downward while W atoms migrate to higher ad layers until the ratio of the top layers turns to be ~3:1. The process of O deposition on W involves a series of sequential substeps, as reported in the literature [62]. Initially, O impacts at 1 eV lack the penetrative power to overcome the

surface barrier of W. However, the adsorbed oxygens bond to the top layer of W and amorphize it, changing the surface potential barrier, and thus opening the doors for incoming oxygen atoms to penetrate below the original W surface, as seen in Fig. 7.

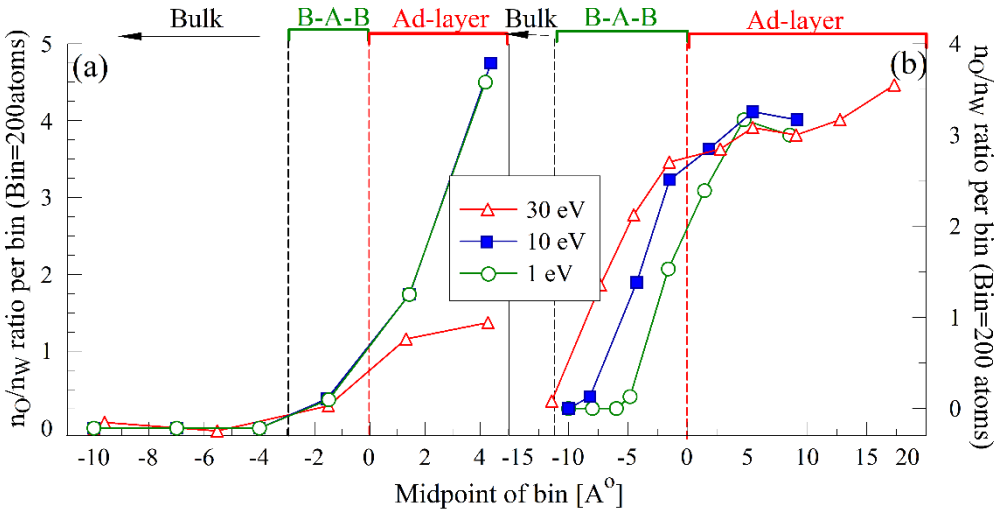

Figure 8 Changes in nO / nW ratios across W (a) "A deps" and (b) "B deps"). Each point represents the average value per bin (bin = 200 atoms of O and W) for 1, 10 and 30 eV. Red dashed lines: Border between the ad-layer and B-A-B regions, black dashed lined: Border between B-A-B and bulk regions.

It is noteworthy that we applied the NVE ensemble constraints to all three O-saturated W systems, 100 picoseconds, to observe the stability of the n_O/n_W ratios. These ratios remained stable over time. WO_3 is recognized as the most stable form of tungsten oxide in the literature [4, 60], however, the n_O:n_W of 3:1 can be maintained by various tungsten and oxygen stoichiometries.

4.2 Role of polarization

One of the factors that causes upward diffusion of W from the bulk to the ad layers is the polarization of the atoms arising from the difference in electronegativities of W (2.36) and O (3.44) on the Pauling scale [63]. The W atoms exhibit positive charges in the regions of the ad layer,

while the O atoms are negatively charged, as shown in Fig. 9. A detailed analysis of the charges through the bins of Fig. S-2 of W slabs and ad-layers is shown in Table S-2 of SM (the charges of the bins in the ad layer (named "+ bins"), the charges of the bins below the original W surface layer in the regions of the BA-B (named "- bins").

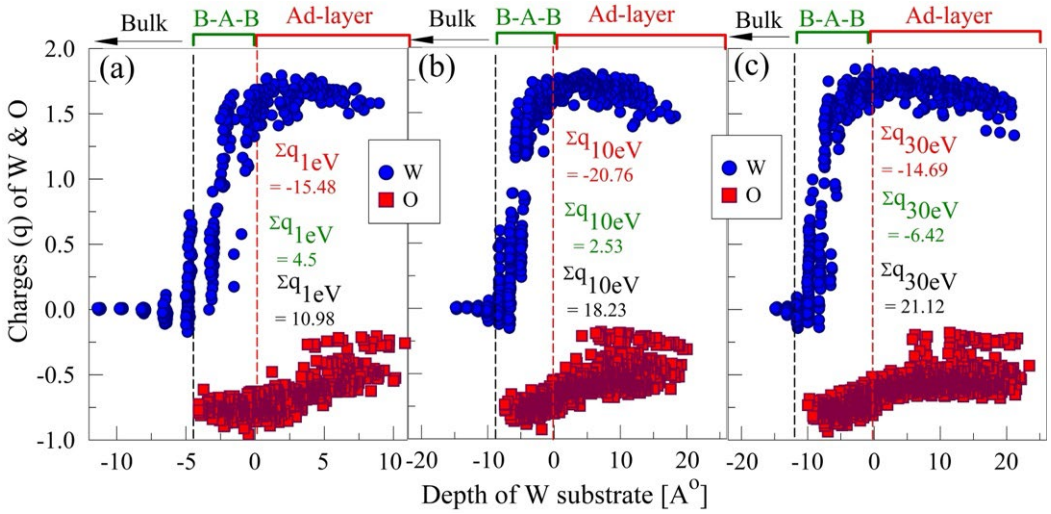

Figure 9: Charges of W and O for O B-deps W substrates 1, 10 and 30 eV O impact energies. Red dashed lines: Border between Ad-layer and B-A-B regions, black dashed lined: Border between B-A-B and bulk regions. $\sum q$: Sum of the charges of the ad-layer bins. $\sum q$: Sum of charges of B-A-B region bins. $\sum q$: Sum of charges of the bulk region.

Fig. 9 also illustrates the sum of charges of W and O in the ad layer, B-A-B, and W bulk region. We can observe a dipolar characteristic between the ad layer and the W slab. Also, the bin-averaged charges of W atoms on the ad layers vary between -0.2 and 1.5, and these keep decreasing as we approach the bulk, falling to almost zero. On the other hand, the oxygen charges in the ad-layers hover around -0.5. A similar pattern was seen and illustrated in Fig. S-3b in SM for O-saturated W substrates. For all energies studied, the average charge of W surged from close to zero in the bulk to approximately 1.7 in the ad-layers due to the high concentration of oxygen in the ad-

layers (the whole system stays charge neutral). The W charges ranged from 0 in the bulk, reaching 1.5 near the B-A-B region. Oxygen charges in the ad layers remained around -0.6, decreasing to -0.8 in the layers beneath the original surface. Remarkably similar average charges are observed across all three cases, suggesting that the O and tungsten charges do not change with the O impact energy. Detailed analysis of the average charges of the W and O atoms is shown in Fig. S-3 in the SM.

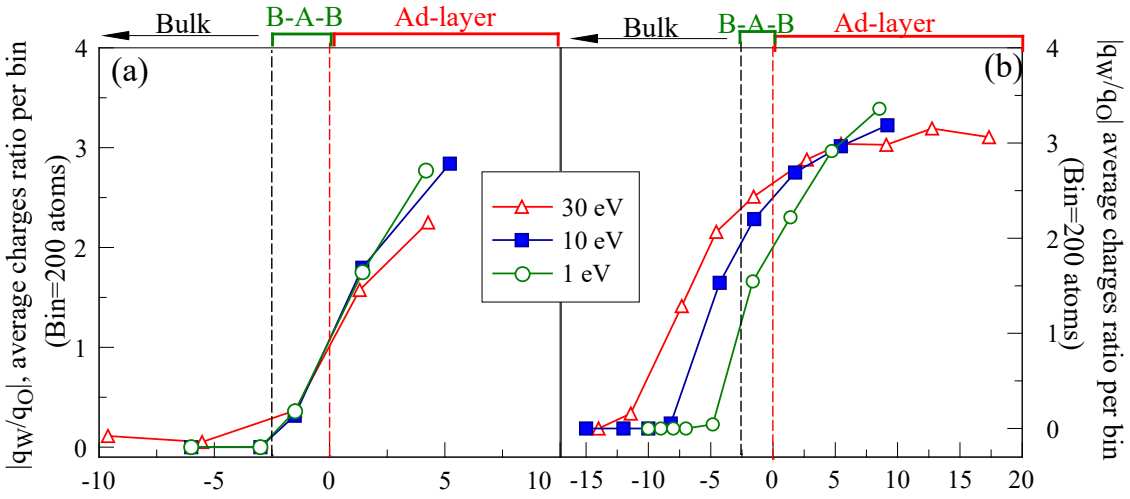

Figure 10: (a) $|q_W/q_O|$ charge ratios for 'A deps' in all W slabs (per bin, bin=200 atoms of O and W) for the impact energies of O 1, 10 and 30 eV. (b) $|q_W/q_O|$ Average charge ratios for 'B deps' throughout the W slabs (per bin, bin=200 atoms of O and W) for the impact energies of O 1, 10 and 30 eV.

Therefore, as mentioned before, we concluded that the n_O/n_W ratio for the adlayer of the three studied W slabs is about 3:1, as illustrated in Fig. 10. Furthermore, we also observed that the average charge ratio $|q_W/q_O|$ for the adlayers in the three W slabs is also approximately 3:1, confirming the possibility of the presence of WO_x molecules, where x~3. W has few possible oxidation states, +6, +5, +4, etc.; however, O always has an oxidation state of -2. Different stoichiometry of tungsten oxide compounds can maintain this charge ratio while maintaining

charge neutrality of the compound. By visualizing a slice of the ad layers of the three studied W slabs, we observe that the tungsten oxide layer is formed of many WO_x compounds linked together in a network, as illustrated in Fig. S-4 in the SM.

4.3 Sputtering during the O-accumulation process

For all three impact energies, 1, 10 and 30 eV, chemical sputtering of W in the form of sputtered WO_x molecules was observed. It is interesting to point out that in all cases, no individual sputtered W atoms were observed; W was always chemically sputtered in the form of W-O compounds, having lower bounding energy to the system than W. In particular, no W was subjected to physical sputtering, consistent with the findings of the literature that the threshold for physical W sputtering of O is 40 eV [7, 8]. Single sputtered O atoms and O_2 molecules were observed. During the irradiation of the W surface by 4500 O atoms of 30 eV, 326 W atoms were sputtered. For the 10 eV O impact case, a total of 72 W atoms were sputtered. In the 1 eV O shots case, 18 W atoms were sputtered. W sputtering for the 10 eV cases commenced after 1000 O impacts (i.e. after deposition of approximately 800 O atoms). After reaching saturation, 3 tungsten atoms are sputtered on average for every 100 O impacts, indicating a tungsten sputtering yield of 0.03 from tungsten oxide ad-layers. On the other hand, after impacts of 1800 O atoms with 30 eV the sputtering of W started after 7.2 ns, with about 15 W atoms sputtered per every 100 O impacts, i.e., the tungsten sputtering yield increases to 0.15. The predominant chemically sputtered species for all three W slabs is WO_4, single O atoms, and O_2 molecules.

Chemically sputtered WO_2 and WO_3 are also observed, but with a smaller frequency than WO_4. When these particles were obtained in the vacuum environment, several molecular decays were observed. Initially, ejected WO_4 caught a single sputtered O atom and was converted into WO_5,

which then decomposed into WO_3 and two single oxygen atoms. Subsequently, WO_3 underwent decomposition into WO_2 and a single oxygen atom. Throughout the simulation, single oxygen atoms and WO_4 continued to form various WO_x compounds [64], such as WO_2, WO_3, WO_4, and WO_5, as well as individual O atoms and O_2 molecules. Fig. 11 is a visualization of the observed sputtered particles along the three-energies O accumulation simulations.

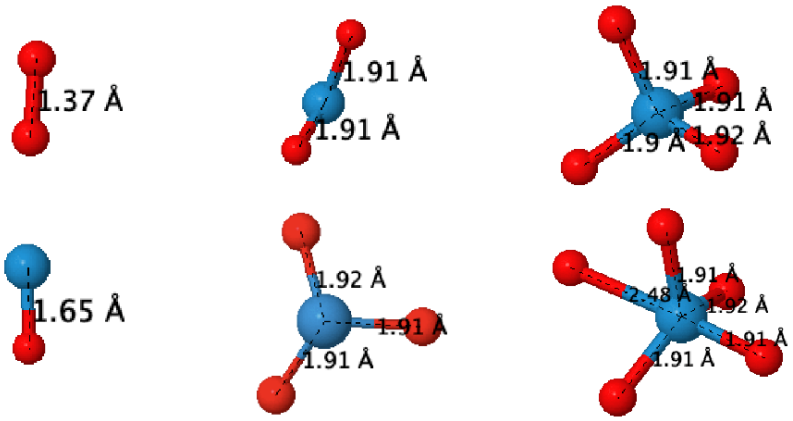

Figure 11: Observed sputtered W-O compounds during the oxygen accumulation process. Blue: W atoms, Red: O atoms.

We observed a notable increase of the sputtered WO_x molecules after reaching saturation of the oxide ad-layers, determined by an impact O energy. The number of WO_x particles sputtered at 30 eV significantly exceeded that at 1eV impact.

4.4 Non-cumulative impacts of O at oxidized layers

We probed the A-deps and B-deps samples created by impacts of 1, 10, and 30 eV by noncumulative O impacts after creating oxidized ad layers by cumulative O irradiation at the respective impact energies. These energies corresponded to the initial O impacts that formed the W-O samples that we utilized. As shown before, we obtained sputtering of W in the form of WO_x

molecules in the cumulative simulations of O upon saturation. To reduce statistical errors, we applied one thousand individual (non-cumulative) impacts at various points of ad layer surfaces. The main goal in this computation was to obtain instantaneous values of the surface parameters, for example, to differentiate between O reflection and sputtering processes, which were not distinguished in the cumulative simulations. We observed only sputtering yields of O atoms. The process of formation and uptake of WO_x that carries chemical sputtering of tungsten is too slow to be detected on a scale of single impact cascade of a few picoseconds. On the other hand, the applied impact energies of O are below the threshold for physical sputtering of tungsten. Thus, the sputtering of tungsten was not seen in the noncumulative irradiation of oxidized tungsten layers.

Table 2 presents the data on reflection, retention, and sputtering for both A-deps and B-deps scenarios following the impact of O atoms. Additionally, it shows the maximal depths reached by 90% of reflected O atoms and the depths from which 90% of sputtered atoms were ejected. No sputtering of O was observed for the 1 eV impact energy. Moreover, the O retention probability (which complements reflection probability to 1) was notably high for 10 and 30 eV impacts. In contrast, for the 1 eV scenario, the retention probability was approximately 50% for the low-O oxide layer, but only 12% for O in a saturated oxide layer. Details of the sputtering and reflection depths for impacted oxygens are illustrated in SI, Figs. S-5 and S-6. For the 10 eV impacts, 90% of the sputtered O atoms were ejected from less than 1Å below the top of the ad layer, that is, from more than 4 Å above the original W surface of the A deps. This implies that the O atoms sputtered from that surface were predominantly ejected from the ad layer. A similar conclusion can be drawn for sputtering of O in the case of B-deps of the 10 eV impact, where O atoms are sputtered from less than about 6 Å below the top ad layer's surface, well above the B-A-B region. Conversely, for the A-deps scenario, for 30 eV with 200 O deposits, most of the sputtered O was ejected from less

Table 2: Retention, reflection, sputtering yield, reflection, and sputtering depths of O atoms resulting from noncumulative, 1000 single O impacts of 1, 10 and 30 eV.

	30eV		10eV		1eV	
	A-deps	B-deps	A-deps	B-deps	A-deps	B-deps
Retention [%]	88 ± 3.0	95.1 ± 3.05	98 ± 0.4	98.5 ± 3.1	49.4 ± 2.2	12.5 ± 1.12
Reflection [%]	12 ± 3.0	5 ± 0.69	2 ± 3.0	1.5 ± 0.38	50.6 ± 2.2	87.5 ± 3.0
Sputtering yield of O [%]	5.3 ± 0.7	6.36 ± 0.79	2.05 ± 0.45	5 ± 0.67	0	0
Reflection depth [Å]	5	8	2	19	1.6	5
Sputtering depth of O[Å]	4	7.5	1	19	--	--

than to 4Å below the top of the ad layer. For the case of 1200 O deposits, approximately 90% of sputtered O atoms were ejected from up to 7.5Å below the top of the ad layer. It can be seen in Table 2 that the reflection depths are close to the corresponding sputtering depths. The oxide ad-layers of tungsten are the source of most of the surface dynamic processes that include uptake of the particles from the tungsten surface, such as reflection and sputtering.

5. CONCLUSIONS

Room temperature irradiation induced oxidation of pure W BCC monocrystal with (001) surface orientation was studied, driven by the impacts of energetic O atoms at 1 eV, 10 eV and 30 eV cumulatively irradiating the surface. The interactions between W and W, O and O, and W and O were described by a newly developed ReaxFF potential, which incorporates bond and charge polarization effects. The developed W-O potential showed excellent agreement with experimental data on cohesive energies, lattice constants, vacancy, and interstitial energies. This potential was used to perform molecular dynamics simulations using LAMPPS.

The incident O atoms create an ad layer, which grows on the W surface, composed of O and W atoms, reaching saturation and an ad layer thickness, which increases with the impact energy. The depth of the oxide subsurface layers also increases with impact energy, although it is thinner and with a deficient oxygen content.

During the irradiation of the W surface by O atoms, oxygen moves toward the bulk, while tungsten migrates upward the surface, reaching an equilibrium number ratio n_O:n_W of 3:1 at the top ad layers. That number decreases to 2:1 in the transitional boundary region between the bulk W and the ad layer, and further decreases inside the oxidized surface until it reaches 0 in the bulk W. These ratios are consistent with the existing literature on the subject. Furthermore, the Mulliken-type charges of the atoms, calculated to simulate the dynamics of polarization of the atoms, follow the same ratios as the number of atoms in the corresponding layers, indicating dominance of particular WO_x molecules in various regions of the oxide. This, for O-saturated layers, x~3 in most of the ad layer, transitioning to x~ 2 in the boundary region, and further decreasing to 1 and less in the subsurface region. The movement of W and O towards each other, forming various stoichiometries in the layers, is influenced by the polarization of the various

layers, leading to ad-layers with a dominantly negative charge and boundary and subsurface regions with a dominantly positive charge.

Upon reaching saturation with O of the ad layers, 18, 72, and 326 W atoms were sputtered from W oxides formed by impact energies of 1, 10, and 30 eV, respectively. However, tungsten is chemically sputtered exclusively in the form of WO_x molecules, which have a lower binding energy to the surface than W. The most probable sputtered particles are WO_4 and atomic oxygen, followed by a chain of dissociations and recombination of the WO_x and single O.

DECLARATION OF INTERESTS

The authors declare that they have no known competing financial or personal interests. relationships that could have appeared to influence the work reported in this paper.

FUNDING

This work is supported by the U.S. Department of Energy, Office of Science/Fusion Energy Sciences under Award Number DE-SC0022013 to Pennsylvania State University.

ACKNOWLEDGMENTS

MS and PK are grateful to ACCESS for allowing use of the SDSC Expanse HPC facility through grant TG-DMR110037.

REFERENCES

[1] Bolt, H., et al. "Materials for the plasma-facing components of fusion reactors." Journal of nuclear materials 329, 66-73. (2004)

[2] Naujoks, D., Asmussen, K., Bessenrodt-Weberpals, M., Deschka, S., Dux, R., Engelhardt, W., ... Wenzel, U. Tungsten as target material in fusion devices. Nuclear fusion, 36(6), 671. (1996)

[3] Pitts, R. A., Carpentier, S., Escourbiac, F., Hirai, T., Komarov, V., Kukushkin, A. S., ... & Stangeby, P. C. Physics basis and design of the ITER plasma-facing components. Journal of Nuclear Materials, 415(1), S957-S964. (2011)

[4] Patnaik, P. Handbook of inorganic chemicals (Vol. 529, pp. 769-771). New York: McGraw-Hill. (2003)

[5] Ivanov, V. E. High temperature oxidation protection of tungsten (Vol. 583). National Aeronautics and Space Administration. (1969)

[6] Davis, J. W., Barabash, V. R., Makhankov, A., Plöchl, L., & Slattery, K. T. Assessment of tungsten for use in the ITER plasma facing components. Journal of nuclear materials, 258, 308-312. (1998)

[7] Landman, I. S., & Wuerz, H. Molecular dynamics simulations of the effect of deuterium on tungsten erosion by oxygen. Journal of nuclear materials, 313, 77-81 (2003)

[8] Matsunami, N., Yamamura, Y., Itikawa, Y., Itoh, N., Kazumata, Y., Miyagawa, S., ... & Tawara, H. Energy dependence of the ion-induced sputtering yields of monatomic solids. Atomic data and nuclear data tables, 31(1), 1-80. (1984)

[9] Gusev, M.I., Korshunov, S.N., Suvorov, A.L. et al. Sputtering of tungsten, tungsten oxide, and tungsten-carbon mixed layers by deuterium ions in the threshold energy region. Tech. Phys. 44, 1123–1127 (1999). https://doi.org/10.1134/1.1259485

[10] Jensen, R. V., Post, D. E., Grasberger, W. H., Tarter, C. B., & Lokke, W. A. Calculations of impurity radiation and its effects on tokamak experiments. Nuclear Fusion, 17(6), 1187. (1977)

[11] Takamura, S., Ohno, N., Nishijima, D., & Kajita, S. Formation of nanostructured tungsten with arborescent shape due to helium plasma irradiation. Plasma and fusion research, 1, 051-051. (2006)

[12] Wu, C. H. Chemical sputtering of graphite and tungsten by oxygen. Journal of Nuclear Materials, 145, 448-452. (1987)

[13] Hirooka, Y., Bourham, M., Brooks, J. N., Causey, R. A., Chevalier, G., Conn, R. W., ... & Ra, Y. Evaluation of tungsten as a plasma-facing material for steady state magnetic fusion devices. Journal of nuclear materials, 196, 149-158. (1992)

[14] Krstić, P. S., Stuart, S. J., & Reinhold, C. O. Chemical Sputtering of Fusion Plasma-Facing Carbon Surfaces. In AIP Conference Proceedings (Vol. 876, No. 1, pp. 201-208). American Institute of Physics (2006)

[15] Nagy, D., & Humphry-Baker, S. A. An oxidation mechanism map for tungsten. Scripta Materialia, 209, 114373. (2022)

[16] Linsmeier, C., Rieth, M., Aktaa, J., Chikada, T., Hoffmann, A., Hoffmann, J., ... & Zhou, Z. Development of advanced high heat flux and plasma-facing materials. Nuclear Fusion, 57(9), 092007. (2017)

[17] Maisonnier, D., Cook, I., Pierre, S., Lorenzo, B., Edgar, B., Karin, B., ... & David, W. The European power plant conceptual study. Fusion Engineering and Design, 75, 1173-1179. (2005)

[18] Dunand, A., Minissale, M., Faure, J. B., Gallais, L., Angot, T., & Bisson, R. Surface oxygen versus native oxide on tungsten: contrasting effects on deuterium retention and release. Nuclear Fusion, 62(5), 054002. (2022)

[19] Hechtl, E., Eckstein, W., Roth, J., & Laszlo, J. Sputtering of tungsten by oxygen at temperatures up to 1900 K. Journal of nuclear materials, 179, 290-293. (1991)

[20] Roth, J., Bohdansky, J., & Ottenberger, W. Data on low energy light ion sputtering. (1979)

[21] Lassner, E., & Schubert, W. D. Tungsten: properties, chemistry, technology of the element, alloys, and chemical compounds. Springer Science & Business Media. (2012)

[22] Senftle, T. P., Hong, S., Islam, M. M., Kylasa, S. B., Zheng, Y., Shin, Y. K., ... & Van Duin, A. C. The ReaxFF reactive force-field: development, applications and future directions. npj Computational Materials, 2(1), 1-14. (2016)

[23] Weismiller, M. R., Van Duin, A. C., Lee, J., & Yetter, R. A. (2010). ReaxFF reactive force field development and applications for molecular dynamics simulations of ammonia borane dehydrogenation and combustion. The Journal of Physical Chemistry A, 114(17), 5485-5492.

[24] Van Duin, A. C., Dasgupta, S., Lorant, F., & Goddard, W. A. (2001). ReaxFF: a reactive force field for hydrocarbons. The Journal of Physical Chemistry A, 105(41), 9396-9409.

[25] Strachan, A., van Duin, A. C., Chakraborty, D., Dasgupta, S., & Goddard III, W. A. (2003). Shock waves in high-energy materials: The initial chemical events in nitramine RDX. Physical Review Letters, 91(9), 098301.

[26] van Duin, A. C., Baas, J. M., & Van De Graaf, B. Delft molecular mechanics: a new approach to hydrocarbon force fields. Inclusion of a geometry-dependent charge calculation. Journal of the Chemical Society, Faraday Transactions, 90(19), 2881-2895. (1994)

[27] Connect with MCC. https://www.mri.psu.edu/materials-computation-center/connect-mcc.

[28] Boda, A., Sk, M. A., Shenoy, K. T., & Mohan, S. Diffusion, permeation and solubility of hydrogen, deuterium and tritium in crystalline tungsten: First principles DFT simulations. International Journal of Hydrogen Energy, 45(53), 29095-29109. (2020)

[29] Ferro, Y., Hodille, E. A., Denis, J., Piazza, Z. A., & Ajmalghan, M. Hydrogen and oxygen on tungsten (110) surface: adsorption, absorption and desorption investigated by density functional theory. Nuclear Fusion, 63(3), 036017. (2023)

[30] Liu, Y. L., Zhang, Y., Luo, G. N., & Lu, G. H. Structure, stability and diffusion of hydrogen in tungsten: A first-principles study. Journal of Nuclear Materials, 390, 1032-1034. (2009)

[31] Johnson, D. F., & Carter, E. A. Hydrogen in tungsten: Absorption, diffusion, vacancy trapping, and decohesion. Journal of Materials Research, 25(2), 315-327. (2010)

[32] Neklyudov, I. M., Sadanov, E. V., Tolstolutskaja, G. D., Ksenofontov, V. A., Mazilova, T. I., & Mikhailovskij, I. M. Interstitial atoms in tungsten: Interaction with free surface and in situ determination of formation energy. Physical Review B, 78(11), 115418. (2008)

[33] Te Velde, G. T., Bickelhaupt, F. M., Baerends, E. J., Fonseca Guerra, C., van Gisbergen, S. J., Snijders, J. G., & Ziegler, T. Chemistry with ADF. Journal of Computational Chemistry, 22(9), 931-967. (2001).

[34] ADF 2023.104, SCM, Theoretical Chemistry, Vrije Universiteit, Amsterdam, The Netherlands. http://www.scm.com.

[35] Perdew, J. P., Burke, K., & Ernzerhof, M. Generalized gradient approximation made simple. Physical review letters, 77(18), 3865. (1996)

[36] Van Lenthe, E., & Baerends, E. J. Optimized Slater-type basis sets for the elements 1–118. Journal of computational chemistry, 24(9), 1142-1156. (2003)

[37] Kresse, G., & Hafner, J. Ab initio molecular dynamics for liquid metals. Physical review B, 47(1), 558. (1993).

[38] Kresse, G.; Joubert, D. From Ultrasoft Pseudopotentials to the Projector Augmented-Wave Method. Phys. Rev. B, 59 (3), 1758–1775. (1999)

[39] Grimme, S., Antony, J., Ehrlich, S., & Krieg, H. (2010). A consistent and accurate ab initio parametrization of density functional dispersion correction (DFT-D) for the 94 elements H-Pu. The Journal of chemical physics, 132(15).

[40] Li, X. C., Shu, X., Liu, Y. N., Gao, F., & Lu, G. H. Modified analytical interatomic potential for a W–H system with defects. Journal of Nuclear Materials, 408(1), 12-17. (2011)

[41] Juslin, N., Erhart, P., Träskelin, P., Nord, J., Henriksson, K. O., Nordlund, K., ... & Albe, K. Analytical interatomic potential for modeling nonequilibrium processes in the W–C–H system. Journal of applied physics, 98(12). (2005)

[42] Shin, Y. K., Gao, Y., Shin, D., & van Duin, A. C. Impact of three-body interactions in a ReaxFF force field for Ni and Cr transition metals and their alloys on the prediction of thermal and mechanical properties. Computational Materials Science, 197, 110602. (2021)

[43] Jain, A., Ong, S. P., Hautier, G., Chen, W., Richards, W. D., Dacek, S., ... & Persson, K. A. Commentary: The Materials Project: A materials genome approach to accelerating materials innovation. APL materials, 1(1). (2013)

[44] de Jong, M., Chen, W., Angsten, T., Jain, A., Notestine, R., Gamst, A., ... & Asta, M. The high-throughput highway to computational materials design. Scientific Data, 2, 150009. (2013)

[45] Mortier, W. J., Ghosh, S. K., & Shankar, S. Electronegativity-equalization method for the calculation of atomic charges in molecules. Journal of the American Chemical Society, 108(15), 4315-4320. (1986)

[46] Stoller, R. E., Tamm, A., Béland, L. K., Samolyuk, G. D., Stocks, G. M., Caro, A., ... & Wang, Y. Impact of short-range forces on defect production from high-energy collisions. Journal of chemical theory and computation, 12(6), 2871-2879. (2016)

[47] Ziegler, J. F., & Biersack, J. P. The stopping and range of ions in matter. In Treatise on heavy-ion science: volume 6: astrophysics, chemistry, and condensed matter (pp. 93-129). Boston, MA: Springer US. (1985)

[48] Kittel, Charles. Introduction to Solid State Physics, seventh.; JohnWiley and Dons. Inc.: New York, NY, (1996)

[49] Lide, D. R. (Ed.). CRC handbook of chemistry and physics (Vol. 85). CRC press. (2004)

[50] Nguyen-Manh, D., Horsfield, A. P., & Dudarev, S. L. Self-interstitial atom defects in bcc transition metals: Group-specific trends. Physical Review B, 73(2), 020101. (2006)

[51] Bolef, D. I., & De Klerk, J. Elastic constants of single-crystal Mo and W between 77° and 500° K. Journal of applied Physics, 33(7), 2311-2314. (1962)

[52] Einarsdotter, K., Sadigh, B., Grimvall, G., & Ozoliņš, V. Phonon instabilities in fcc and bcc tungsten. Physical review letters, 79(11), 2073. (1997)

[53] Morse, M. D. Clusters of transition-metal atoms. Chemical Reviews, 86(6), 1049-1109. (1986)

[54] Rasch, K. D., Siegel, R. W., & Schultz, H. (1980). Quenching and recovery investigations of vacancies in tungsten. Philosophical Magazine A, 41(1), 91-117.

[55] Thompson, A. P., Aktulga, H. M., Berger, R., Bolintineanu, D. S., Brown, W. M., Crozier, P. S., ... & Plimpton, S. J. LAMMPS-a flexible simulation tool for particle-based materials modeling at the atomic, meso, and continuum scales. Computer Physics Communications, 271, 108171. (2022)

[56] Expanse: http://expanse.sdsc.edu.

[57] Roar Supercomputer (ICDS): https://www.icds.psu.edu/

[58] Gomer, R., & Hulm, J. K. Adsorption and diffusion of oxygen on tungsten. The Journal of Chemical Physics, 27(6), 1363-1376. (1957)

[59] McCarroll, B. Chemisorption and oxidation: oxygen on tungsten. The Journal of Chemical Physics, 46(3), 863-869. (1967)

[60] Baur, J. P., Bridges, D. W., & Fassell, W. M. High pressure oxidation of metals—Tungsten in oxygen. Journal of The Electrochemical Society, 103(5), 266. (1956)

[61] Webb, W. W., Norton, J. T., & Wagner, C. Oxidation of tungsten. Journal of The Electrochemical Society, 103(2), 107. (1956)

[62] Wendel, J. Thermodynamics and kinetics of tungsten oxidation and tungsten oxide sublimation in the temperature interval 200–1100 C. Diploma work. (2014).

[63] L. Pauling, The nature of the chemical bond. IV. The energy of single bonds and the relative electronegativity of atoms, J. Am. Chem. Soc. 54, 357 (1932).

[64] Zhai, H. J., Kiran, B., Cui, L. F., Li, X., Dixon, D. A., & Wang, L. S. (2004). Electronic Structure and Chemical Bonding in MO n-and MO n Clusters (M= Mo, W; n= 3− 5): A Photoelectron Spectroscopy and ab Initio Study. Journal of the American Chemical Society, 126(49), 16134-16141.